INORGANIC CHEMISTRY

FRONTIERS

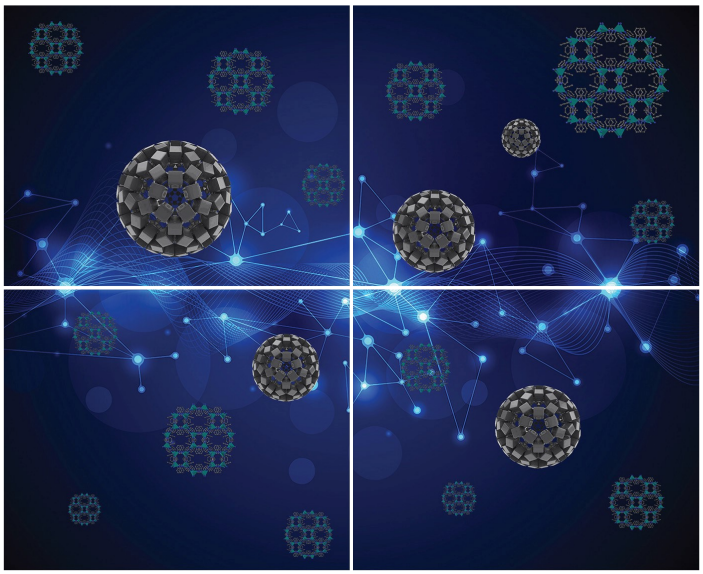

Accepted Manuscript

This article can be cited before page numbers have been issued, to do this please use: Y. Xiang, H. Wang, S. Li, L. Li, J. Ren, G. Xing, L. Deng and S. Peng, *Inorg. Chem. Front.*, 2026, DOI: 10.1039/D5QI02279G.

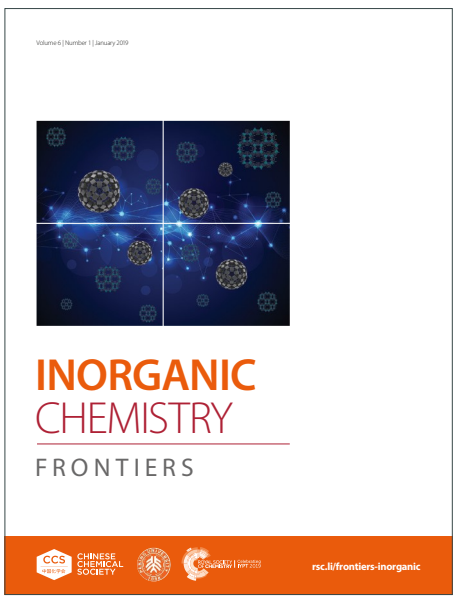

View Article Online
DOI: 10.1039/D5QI02279G

ARTICLE

Oxygen-bridged electronic coupling of Ir single-atom sites for durable acidic oxygen evolution reaction

Received 00th January 20xx,
Accepted 00th January 20xx

DOI: 10.1039/x0xx00000x

Yijun Xiang,[a] Hui Wang,[b] Shaoxiong Li,[a] Linlin Li,[a] Jianwei Ren,[c] Gengyu Xing,*[a] Liming Deng,*[a] and Shengjie Peng*[d]

Developing stable and efficient single-atom electrocatalysts for the acidic oxygen evolution reaction (OER) is crucial for advancing proton exchange membrane water electrolysis (PEMWE). However, the lack of precisely tailored coordination environments capable of preventing noble metal single-atom dissolution remains a critical barrier. Herein, we construct Ir single-atom catalysts supported on Co_3O_4 (Ir_{SA}-Co_3O_4) via the synchronized formation of cobalt defects and the immobilization of Ir single atoms during precursor pyrolysis. Atomically dispersed Ir atoms are anchored at octahedral cobalt defect sites, forming a configuration of single atoms confined within the spinel lattice. Benefiting from the oxygen-bridged electronic coupling within the Ir–O–Co configuration, the electronic structure of Ir sites is optimized to enable moderate intermediate adsorption while mitigating dissolution during acidic OER. As a result, Ir_{SA}-Co_3O_4 achieves a low overpotential of 199 mV at 10 mA cm^{-2} in 0.5 M H_2SO_4 and operates stably for 150 h at 200 mA cm^{-2} in PEMWE. This work provides new insights into the rational design of stable single-atom catalysts for acidic OER by effectively suppressing active-site dissolution.

Introduction

Hydrogen (H_2), characterized by its high energy density and zero carbon emissions, is widely regarded as a viable alternative to fossil fuels.[1-3] Among the various routes for green hydrogen production, proton exchange membrane water electrolysis (PEMWE) powered by renewable energy stands out as particularly promising.[4-7] The overall efficiency of PEMWE critically depends on the development of highly active and durable catalysts for the oxygen evolution reaction (OER) under acidic conditions.[8-10] Iridium (Ir)-based materials remain the benchmark anode catalysts due to the exceptional durability of Ir under the corrosive and oxidizing environment of acidic OER.[11-13] However, the high cost and limited availability of Ir necessitate reducing Ir loading by at least an order of magnitude to enable scalable industrial application.[14-16] Consequently, the development of cost-effective catalysts with optimized architectures that minimize Ir loading without compromising catalytic performance remains an urgent necessity and a formidable challenge.

Currently, single-atom catalysts (SACs), with atomic-level dispersion and finely tuned coordination environments, have attracted growing attention by maximizing noble metal utilization and enabling tailored electronic structures.[17-20] An ideal support for SACs is expected to integrate structural stability with high electrical conductivity, thereby suppressing unnecessary energy consumption and catalyst deactivation under operating voltages.[21-23] Among various metal oxide supports, spinel cobalt oxide (Co_3O_4) stands out for its pseudocapacitive characteristics, which originate from mixed-valence cobalt centers and facile redox transitions, along with moderate acid stability.[24-26] More importantly, the tunable electronic states of Co_3O_4 provide favorable conditions for regulating the electronic structure of Ir single atoms through electronic interactions.[27-29] Ir atoms hybridize with coordinated oxygen, and the mediation occurs through oxygen atoms in the second coordination shell associated with Co. The oxygen-bridged electronic coupling within the Ir–O–Co configuration is expected to modulate the electronic structure of Ir and thereby influence intermediate adsorption and dissolution behavior, ultimately impacting OER activity and stability.[30, 31] Recent studies have shown that differences in electronic interactions, arising from distinct coordination environments of single atoms loaded on the same support, are closely related to variations in catalytic performance.[32-34] As the coordination environment is inherently determined by the anchoring sites, a precise definition of single-atom sites becomes crucial for tailoring their electronic states and ensuring desirable catalytic performance.[35, 36] However, achieving accurate anchoring of Ir single atoms in Co_3O_4 remains a major barrier, owing to insufficient lattice compatibility and the

[a] College of Materials Science and Technology, Nanjing University of Aeronautics and Astronautics, Nanjing 210016, China. E-mail: gengyuxing950308@163.com, limingdeng@nuaa.edu.cn
[b] Xi'an Aerospace Propulsion Institute, Xi'an 710100, China.
[c] Department of Chemical Engineering, University of Pretoria, Pretoria 0028, South Africa.
[d] School of Energy and Environment & Z Energy Storage Center, Southeast University, Nanjing 211189, China. E-mail: pengshengjie@seu.edu.cn
Electronic Supplementary Information (ESI) available. See DOI: 10.1039/x0xx00000x

DOI: 10.1039/D5QI02279G

thermally driven aggregation of Ir during calcination.[37] In addition, oxygen defects formed during calcination may cause surface adsorption of Ir species, preventing the establishment of the desired coordination environments and producing electronic states that are misaligned with the targeted catalytic behavior.[38] Overcoming the above obstacles is expected to secure well-defined anchoring sites and establish favorable coordination environments for Ir single atoms, ultimately enabling high-performance acidic OER.

In this work, Ir single-atom catalysts supported on Co_3O_4 (Ir_{SA}-Co_3O_4) with uniformly dispersed single-atom sites are constructed through a defect-mediated anchoring strategy. The in-situ formation of cobalt defects provides anchoring sites for isolated Ir atoms, leading to a spatially defined Ir–O–Co coordination structure that modulates the electronic states of Ir. Density functional theory (DFT) calculations indicate that an optimized coordination environment tunes the adsorption energies of key OER intermediates, thereby enhancing catalytic activity. The oxygen-bridged Ir–O–Co electronic coupling modulates the electronic structure of Ir and suppresses Ir dissolution, contributing to the stability of Ir_{SA}-Co_3O_4. Consequently, Ir_{SA}-Co_3O_4 delivers a low overpotential of 199 mV at 10 mA cm^{-2} and maintains stable operation for over 300 h. Notably, Ir_{SA}-Co_3O_4 sustains continuous operation for 150 h at 0.2 A cm^{-2} in PEMWE, indicating the potential for practical application. This work provides new insights into the design of high-performance PEMWE catalysts and serves as a valuable reference for the rational development of SACs.

Experimental section

Chemicals and materials

Glycerol ($C_3H_8O_3$, 99%) and hexachloroiridic acid hydrate ($H_2IrCl_6 \cdot xH_2O$, 99%) were purchased from Aladdin. Cobalt(II) acetate anhydrous ($(CH_3COO)_2Co$, 98%) and Sodium hydroxide (NaOH, 95%) were purchased from Sinopharm Chemical Reagent Co. Commercial Iridium(IV) oxide (IrO_2, 99%) was purchased from Macklin. Commercial Pt/C (40 wt% Pt) catalyst was purchased from Sigma-Aldrich.

Synthesis of cobalt glycerolate (Co-gly)

Anhydrous cobalt acetate ($(CH_3COO)_2Co$, 1.0 g) was dissolved in 30 mL of glycerol and magnetically stirred for 2 h to obtain a uniform purple suspension. The resulting mixture was sealed in a 40 mL Teflon-lined autoclave and maintained at 180 °C for 2 h. The viscous product was separated by centrifugation, repeatedly rinsed with ethanol until the surface became non-sticky, and then dried under vacuum at 60 °C overnight to obtain a pink powder.

Synthesis of Co_3O_4

The obtained Co-gly precursor was calcined in air at 300 °C and 700 °C for 4 h to yield Co_3O_4-300 and Co_3O_4-700, as shown in Fig. S11.

Synthesis of Ir_{SA}-Co_3O_4 (Ir single-atom anchored cobalt oxides)

Co-gly (50 mg) was dispersed in an ethanolic solution of 5 mM $H_2IrCl_6 \cdot xH_2O$, and the pH of the suspension was tuned to neutral by adding NaOH. After impregnation and continuous stirring at room temperature for 14 h, the solid was recovered via centrifugation, washed several times with ethanol, dried under vacuum, and finally calcined in air at 300 °C for 4 h to yield Ir_{SA}-Co_3O_4. Samples prepared with 1, 3, 5, and 7 mM $H_2IrCl_6 \cdot xH_2O$ were denoted as Ir-Co_3O_4-1, Ir-Co_3O_4-3, Ir-Co_3O_4-5, and Ir-Co_3O_4-7, respectively, as shown in Fig. S12.

Synthesis of Ir_{ACSA}-Co_3O_4 (cobalt oxides with Ir single atoms and atomic clusters)

The synthesis procedure was identical to that of Ir_{SA}-Co_3O_4, except that the resulting precursor was heat-treated at 700 °C for 4 h in a muffle furnace. The elevated temperature led to partial aggregation of isolated Ir atoms into small clusters, yielding a catalyst containing both Ir atomic clusters (AC) and single atoms (SA), designated as Ir_{ACSA}-Co_3O_4.

Material characterization

The catalyst morphologies were examined by scanning electron microscopy (SEM, Hitachi Regulus 8100). Transmission electron microscopy (TEM) and high-resolution TEM (HR-TEM) were conducted on a Tecnai G2 F20 (FEI, 200 kV). Elemental compositions were analyzed by inductively coupled plasma optical emission spectroscopy (ICP-OES, Optima 7300 DV). The crystalline phases were identified by X-ray diffraction (XRD, Bruker D8 Discover) with Cu Kα radiation (λ = 1.5418 Å). X-ray photoelectron spectroscopy (XPS, ESCALAB 250Xi) using Al Kα radiation was employed to determine surface chemical states, and all binding energies were calibrated to the C 1s peak at 284.8 eV. Raman spectra were collected on a DXR confocal microscope (532 nm laser), while electron paramagnetic resonance (EPR, Bruker A300) was used to probe cationic defects. Extended X-ray absorption fine structure (EXAFS) and X-ray absorption near-edge structure (XANES) measurements at the Co K-edge and Ir L_3-edge were performed at beamline TPS 44A1 (NSRRC, Hsinchu, Taiwan) and analyzed using the Athena software.

Electrochemical measurements

Electrochemical tests were carried out in a three-electrode setup, employing a Pt plate as the counter electrode and a saturated Ag/AgCl (KCl) electrode as the reference. During ambient conditions, measurements were performed on an Autolab workstation (Autolab Instrument). The catalyst powder, carbon black, and polyvinylidene fluoride (PVDF) binder were combined in a mass ratio of 7:2:1, with N-methyl-2-pyrrolidone (NMP) as the dispersing solvent. The catalyst loading on carbon paper was controlled at approximately 0.5 mg cm^{-2}.

PEMWE measurements

View Article Online
DOI: 10.1039/D5QI02376C

Membrane electrode assemblies (MEAs) were fabricated using the catalyst-coated membrane (CCM) technique with Nafion 115 membranes (2 × 2 cm^2). Ir_{SA}-Co_3O_4, Ir_{ACSA}-Co_3O_4, and IrO_2 were employed as anode catalysts, while Pt/C was applied at the cathode. Catalyst inks were prepared by dispersing the powders in isopropanol, deionized water, and a 5 wt% Nafion ethanol solution, followed by spraying onto both sides of the membrane via the PTFE transfer method. The total catalyst loading was maintained at 2.0 mg cm^{-2} for all electrodes. Titanium felt was used as the anode gas diffusion layer (GDL), and carbon paper as the cathode GDL. The catalyst-coated membrane and GDLs were hot-pressed at 130 °C under 10 MPa for 5 min. A peristaltic pump delivered Pure water to both anode and cathode chambers at 40 rpm.

Theoretical calculation

DFT calculations were conducted using the Vienna ab initio Simulation Package (VASP) with the projector-augmented wave (PAW) method and the Perdew-Burke-Ernzerh (PBE) functional under the generalized gradient approximation (GGA). For cobalt oxides, the Hubbard U correction (U_{eff} = 3.32 eV) was applied. A plane-wave cutoff of 500 eV and a 3 × 3 × 1 Monkhorst-Pack k-point grid were used. All structures were spin-polarized and fully relaxed until the total energy and residual forces converged to 10^{-5} eV per atom and below 0.05 eV $Å^{-1}$.

Results and discussion

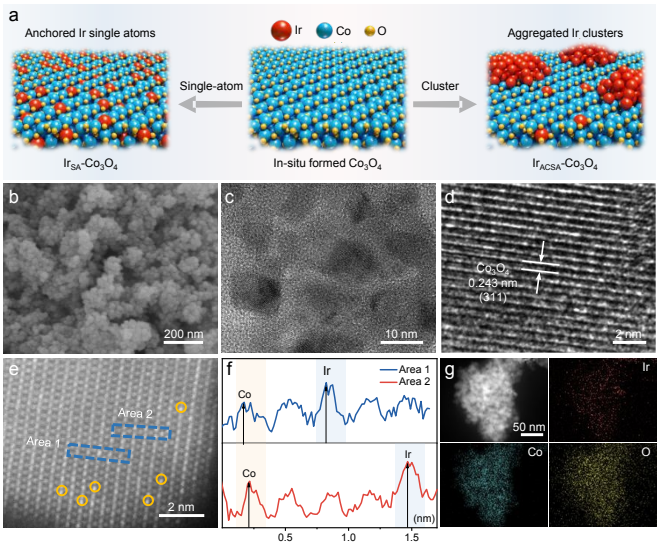

Fig. 1. Characterization of Ir single atoms anchored on Co_3O_4. (a) Schematic illustration of single-atom loading (Ir_{SA}-Co_3O_4) and cluster-involved loading (Ir_{ACSA}-Co_3O_4) on in-situ formed Co_3O_4. (b) SEM, (c) TEM, (d) HR-TEM, and (e) HAADF-STEM images of Ir_{SA}-Co_3O_4. (f) The corresponding intensity profiles of Co_3O_4 along the dashed rectangles in (e) highlight the isolated distribution of Ir atoms. (g) Elemental mapping of Ir_{SA}-Co_3O_4 obtained by TEM shows the spatial distribution of Ir, Co, and O.

As illustrated in Fig. 1a, a defect-mediated anchoring strategy was adopted to construct Ir_{SA}-Co_3O_4, in which Ir single atoms are precisely anchored at cobalt defects. During thermal treatment of the Co-gly precursor, the oxygen-rich atmosphere promoted the formation of cobalt defects that act as anchoring sites for atomically dispersed Ir (Figs. S1 and S2). To clarify the role of single-atom coordination environments in catalytic performance, a reference catalyst containing both Ir atomic clusters and single atoms supported on Co_3O_4 (Ir_{ACSA}-Co_3O_4) was synthesized for comparison (Fig. S3). Ir_{SA}-Co_3O_4 consists of uniformly sized nanoparticles with an average diameter of approximately 11 nm (Figs. 1b and c). Distinct lattice fringes are observed in individual nanoparticles (Fig. 1d), corresponding to the (311) plane of the Co_3O_4 lattice with an interplanar spacing of 0.243 nm.[39, 40] High-angle annular dark-field scanning transmission electron microscopy (HAADF-STEM) images of Ir_{SA}-Co_3O_4 reveal atomically ordered Co arrays (Fig. 1e). Some brighter atomic columns are assigned to Ir atoms, as further verified by the intensity profiles taken from representative regions (Fig. 1f). The absence of aggregated Ir clusters suggests that Ir atoms are predominantly incorporated into lattice sites of Co_3O_4. Elemental mapping (Fig. 1g) further confirms the homogeneous spatial distribution of Ir, Co, and O throughout the catalyst. These results collectively indicate that Co defects within the –Co–O–Co– framework act as effective trapping sites during pyrolysis, enabling the formation of lattice-confined Ir atoms. Notably, incorporation of Ir into specific lattice sites can modulate the local electronic structure of Ir sites and thereby influence the catalytic behavior of Ir_{SA}-Co_3O_4.

Given the ultralow Ir loading (Table S1), both Ir_{SA}-Co_3O_4 and Ir_{ACSA}-Co_3O_4 preserve the spinel framework without detectable lattice disruption. The XRD patterns of Ir_{SA}-Co_3O_4 and Ir_{ACSA}-Co_3O_4 are imperceptibly shifted relative to pristine Co_3O_4 (Fig. 2a). Notably, metallic Ir peaks are absent in Ir_{SA}-Co_3O_4, consistent with isolated Ir species stabilized at Co defects without aggregation. In contrast, Ir_{ACSA}-Co_3O_4 displays reflections attributable to metallic Ir, indicating that the applied high-temperature calcination promoted Ir aggregation, thereby providing a reference sample lacking tailored coordination environments for Ir sites. EPR spectra (Fig. S4) reveal a distinct signal at g = 2.004, typically associated with Co vacancies.[26] Compared to pristine Co_3O_4, Ir_{SA}-Co_3O_4 exhibits a markedly weaker signal, which further supports that the defect-mediated incorporation strategy stabilizes isolated Ir atoms within the lattice. Raman analysis reveals a red shift of the characteristic bands in Ir_{SA}-Co_3O_4 relative to pristine Co_3O_4 (Fig. S5). Notably, the A_{1g} band (~668 cm^{-1}), which is highly sensitive to vibrational changes of octahedral sites, shows a more pronounced shift compared to the F_{2g} bands that originate from tetrahedral sites. This distinct difference implies that Ir atoms preferentially substitute for octahedral rather than tetrahedral positions, as further illustrated by the structural modeling in Fig. S6.[41] Thermogravimetric (TG) analysis (Fig. S7) shows that Ir incorporation modifies the thermal decomposition profile of the Co-gly precursor. Compared with the abrupt mass loss of Co-gly, Ir-loaded Co-gly (Ir-Co-gly) exhibits a more gradual decomposition behavior, indicating a moderated thermal process. This behavior is consistent with the formation of Co defects, which can subsequently act as anchoring sites for isolated Ir atoms during calcination.

The valence states of the surface metal species were influenced by Ir anchoring, as revealed by XPS, demonstrating

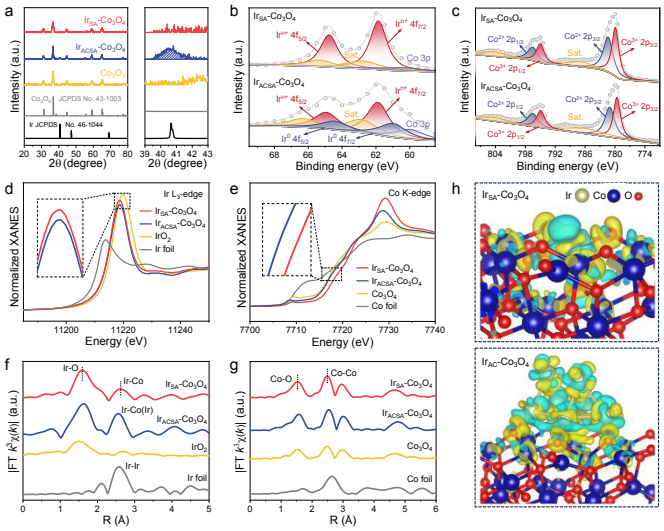

Fig. 2. Structure and electronic features of Ir_{SA}-Co_3O_4 and Ir_{ACSA}-Co_3O_4. (a) XRD patterns of Ir_{SA}-Co_3O_4, Ir_{ACSA}-Co_3O_4, and Co_3O_4. The enlarged region highlights the (111) peak of Ir observed in Ir_{ACSA}-Co_3O_4. (b) Ir 4f and (c) Co 2p XPS spectra of Ir_{SA}-Co_3O_4 and Ir_{ACSA}-Co_3O_4. (d) Normalized Ir L_3-edge XANES of Ir_{SA}-Co_3O_4, Ir_{ACSA}-Co_3O_4, IrO_2, and Ir foil. (e) Normalized Co K-edge XANES of Ir_{SA}-Co_3O_4, Ir_{ACSA}-Co_3O_4, Co_3O_4, and Co foil. (f) FT-EXAFS spectra corresponding to (d). (g) FT-EXAFS spectra corresponding to (e). (h) Differential charge density of Ir_{SA}-Co_3O_4 and Ir_{AC}-Co_3O_4 models, constructed to clearly distinguish the differences in electronic interactions. Cyan and yellow regions represent electron depletion and accumulation, respectively.

the distinct electronic environments of Ir_{SA}-Co_3O_4 and Ir_{ACSA}-Co_3O_4 (Figs. 2b and c). The electronic coupling within Ir–O–Co configurations modulates the electronic states of both the Ir and Co elements. Ir sites possess an increased electron density, which is confirmed by a reduced oxidation state (Ir^{n+}, $n < 4$) and evidenced by a 0.26 eV negative shift of the Ir $4f_{7/2}$ binding energy relative to IrO_2 (Fig. S8a).[42] The Co 2p spectrum further corroborates this interaction, with the Co^{3+} fraction increasing from 42.2% in pristine Co_3O_4 to 50.5% in Ir_{SA}-Co_3O_4, thereby evidencing oxidation of surface Co species (Fig. S8b). Collectively, these spectroscopic results reveal a redistribution of electron density involving Co and anchored Ir sites, indicative of electronic coupling between the support and isolated Ir atoms. In contrast, Ir_{ACSA}-Co_3O_4 exhibits a Co^{3+} fraction of ~45.3%, reflecting weaker electronic interactions and a less pronounced reduction of the Ir^{n+} state (Fig. S9).

X-ray absorption spectroscopy (XAS) further demonstrated an intrinsic link between electronic coupling and the coordination environment of atomically anchored Ir in Ir_{SA}-Co_3O_4. In the Ir L_3-edge XANES spectra (Fig. 2d), the white-line intensity of Ir_{SA}-Co_3O_4 was lower than that of IrO_2, indicating an oxidation state below +4.[31] The Ir L_3-edge Fourier-transformed EXAFS (FT-EXAFS) spectrum (Fig. 2f) displayed only Ir–O coordination in the first shell and no detectable Ir–Ir contribution at ~2.7 Å.[43] Consistently, wavelet-transform (WT) analysis (Fig. S10a) showed a distinct low-k feature (~5 $Å^{-1}$) characteristic of Ir–O scattering without any high-k Ir–Ir signal, together confirming the precise atomic-level dispersion of Ir. The reduced population of unoccupied Ir 5d states further demonstrated that the strong electronic coupling with the support stemmed from the well-defined coordination of atomically anchored Ir. On the support side, the Co K-edge XANES (Fig. 2e) exhibited a positively shifted absorption edge relative to pristine Co_3O_4, indicative of an increased oxidation state of interfacial Co species.[44] The corresponding FT-EXAFS (Fig. 2h) showed nearly unchanged Co–O and Co–Co coordination, demonstrating that although electron redistribution occurred, the spinel lattice framework remained intact.[35] In contrast, Ir_{ACSA}-Co_3O_4 exhibited pronounced Ir–Ir contributions in the Ir L_3-edge FT-EXAFS (Fig. 2f), with a clear peak at 2.7 Å that was absent in Ir_{SA}-Co_3O_4. WT analysis (Fig. S10b) further revealed a vigorous high-k intensity (~10 $Å^{-1}$) attributable to Ir–Ir scattering, in conjunction with the relatively weaker white-line intensity in the XANES (Fig. 2d), confirming the aggregation of Ir atoms. The absence of well-defined Ir–O–Co configurations weakened the electronic coupling between Ir and interfacial Co species, as reflected by the minimal Co-edge shift (Fig. 2e).

DFT calculations were employed to investigate charge redistribution near Ir sites, as governed by distinct coordination configurations formed with Co_3O_4 (Fig. 2h). To control for effects arising from coordination-structure differences, we constructed an idealized model consisting of Ir atomic clusters supported on Co_3O_4 (Ir_{AC}-Co_3O_4). In Ir_{SA}-Co_3O_4, the differential charge density reveals pronounced electron redistribution within the Ir–O–Co configuration, characterized by electron depletion at the Ir site and accumulation on the adjacent oxygen atoms. By contrast, Ir_{AC}-Co_3O_4 exhibits weaker interfacial coupling, and Bader charge analysis yielded a total interfacial charge loss of 1.76 e^- (0.35 e^- per atom). This value is significantly lower than the 1.54 e^- observed for Ir_{SA}-Co_3O_4, indicating diminished Ir-centered electronic interactions owing to the absence of well-defined Ir–O–Co configurations. Theoretical calculations together with spectroscopic analyses consistently demonstrate that atomically anchored Ir, stabilized by a defined coordination structure, engages in stronger electronic coupling that is expected to influence catalytic performance.

To investigate the influence of electronic interactions on catalytic performance, we evaluated the OER activity of the catalysts in a three-electrode system using 0.5 M H_2SO_4 as the electrolyte. As shown in Fig. 3a, Ir_{SA}-Co_3O_4 required an overpotential of only 199 mV (η) to reach 10 mA cm^{-2}, markedly lower than Ir_{ACSA}-Co_3O_4 (255 mV) and commercial IrO_2 (285 mV). Moreover, the OER activity is predominantly determined by the Ir sites, with the Co_3O_4 support providing only a minor contribution (Fig. S11). Nevertheless, increasing the Ir precursor concentration beyond the coordination capacity of the support does not yield additional performance improvement (Fig. S12), indicating that the number of accessible anchoring sites becomes saturated. In addition, Ir_{SA}-Co_3O_4 exhibited the lowest Tafel slope of 56.5 mV dec^{-1} (Fig. 3b), indicating accelerated OER kinetics and consistent with the minimal charge-transfer resistance revealed by electrochemical impedance spectroscopy (EIS, Figs. S13a-c). Cyclic voltammetry in the non-Faradaic region was used to estimate the electrochemically active surface area (ECSA, Figs. S14a-c). Ir_{SA}-Co_3O_4 exhibited the largest double-layer capacitance of 156.2 mF cm^{-2} (Fig. 3c), corresponding to an increased electrochemically active surface area derived from atomic-scale Ir dispersion. After ECSA

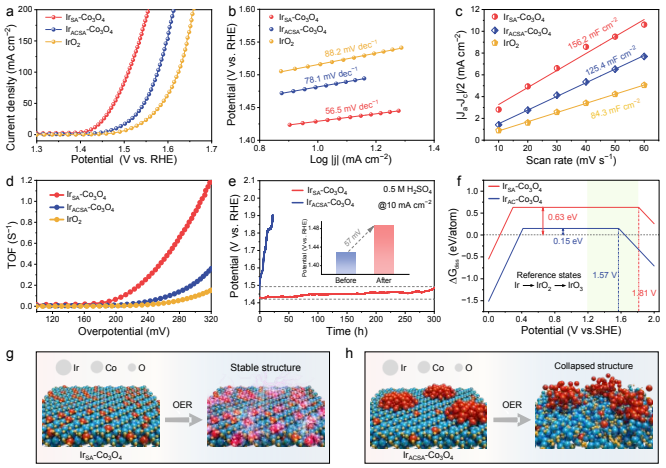

Fig. 3. OER activity and stability of Ir_{SA}-Co_3O_4. (a) LSV polarization curves and (b) Tafel slopes of Ir_{SA}-Co_3O_4, Ir_{ACSA}-Co_3O_4, and IrO_2. (c) C_{dl} plots obtained from the CV curves. (d) TOF plots of Ir_{SA}-Co_3O_4, Ir_{ACSA}-Co_3O_4, and IrO_2. (e) Chronopotentiometry curves at 10 mA cm^{-2} in a 0.5 M H_2SO_4 electrolyte. (f) DFT-calculated free-energy diagrams of Ir_{SA}-Co_3O_4 and Ir_{AC}-Co_3O_4 at pH = 0, referenced to Ir → IrO_2 → IrO_3 states, illustrating the dissolution free energy (ΔG_{diss}) as a function of applied potential. (g, h) Schematic illustrations of structural evolution under acidic OER conditions. Ir_{SA}-Co_3O_4 maintains structural integrity, while Ir_{ACSA}-Co_3O_4 undergoes structural collapse.

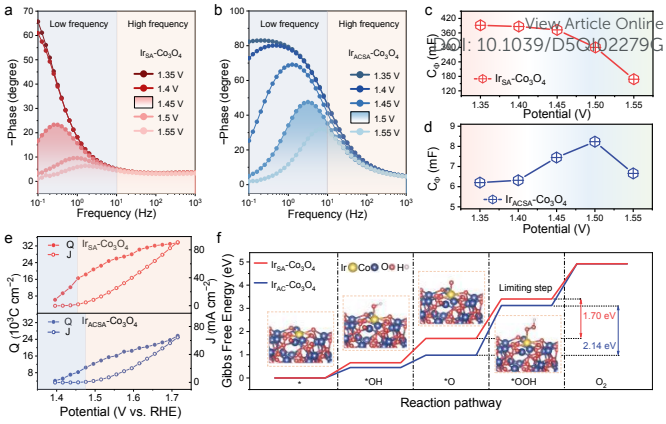

Fig. 4. Kinetic analysis of Ir_{SA}-Co_3O_4 during acidic OER. (a, b) Bode plots of Ir_{SA}-Co_3O_4 and Ir_{ACSA}-Co_3O_4 at different applied potentials. (c, d) Interfacial capacitance values of Ir_{SA}-Co_3O_4 and Ir_{ACSA}-Co_3O_4 as a function of applied potential, derived from EIS. (e) Accumulated charge (Q) and current density (J) versus potential for Ir_{SA}-Co_3O_4 and Ir_{ACSA}-Co_3O_4, obtained from pulse voltammetry. (f) Gibbs free energy diagrams of OER on Ir_{SA}-Co_3O_4 and Ir_{AC}-Co_3O_4 at 0 V (vs. NHE).

normalization, Ir_{SA}-Co_3O_4 still delivered higher current densities at given overpotentials than Ir_{ACSA}-Co_3O_4 and IrO_2 (Fig. S15). Moreover, Ir_{SA}-Co_3O_4 achieved superior noble metal utilization, as reflected by its highest mass activity after normalization to Ir content (Fig. S16). Collectively (Fig. S17), these results demonstrate that the performance of Ir_{SA}-Co_3O_4 cannot be attributed solely to enlarged surface area or increased site density, but instead originates from enhanced intrinsic activity. Consistently, turnover frequency (TOF) analysis (Fig. 3d) showed that Ir_{SA}-Co_3O_4 reached 0.9 s^{-1} at 300 mV, far exceeding Ir_{ACSA}-Co_3O_4 and IrO_2. Taken together, the above data demonstrate that the well-defined Ir–O–Co coordination environment created by single-atom anchoring enhances the intrinsic activity of Ir_{SA}-Co_3O_4.

Long-term stability was evaluated at a constant current density of 10 mA cm^{-2} in 0.5 M H_2SO_4 (Fig. 3e). Ir_{SA}-Co_3O_4 maintained a nearly steady potential for over 300 h, with only a minor 57 mV increase during continuous operation. We carried out DFT calculations to assess the dissolution free energy of Ir species at operating potentials, thereby probing the basis for the resistance of Ir_{SA}-Co_3O_4 to dissolution.[45] The results indicate that Ir_{SA}-Co_3O_4 possesses a much larger dissolution margin (0.63 eV/atom) than Ir_{AC}-Co_3O_4 (0.15 eV/atom), corresponding to an additional 0.48 eV per atom of thermodynamic resistance against dissolution. Furthermore, the instability onset is shifted from 1.57 V in Ir_{AC}-Co_3O_4 to 1.81 V in Ir_{SA}-Co_3O_4, thus extending the stability window throughout the acidic OER regime (Fig. 3f). After OER stability testing, Ir dissolution was limited to 0.74% for Ir_{SA}-Co_3O_4, markedly lower than the 5.41% measured for Ir_{ACSA}-Co_3O_4 (Fig. S18). The agreement between experiment and theory confirms that electronic interactions, facilitated by the tailored coordination environment, mitigate Ir dissolution and preserve stability in acidic OER. In Ir_{SA}-Co_3O_4, Ir atoms anchored at cobalt defect sites help preserve the Co_3O_4 framework and prevent structural collapse during extended electrolysis (Fig. 3g). In contrast, Ir species in Ir_{ACSA}-Co_3O_4 lack sufficient coordination stabilization, which accelerates breakdown of the spinel lattice under oxidative conditions (Fig. 3h). Post-OER SEM images further support this structural divergence: Ir_{SA}-Co_3O_4 retains a largely preserved morphology (Fig. S19), whereas Ir_{ACSA}-Co_3O_4 exhibits pronounced structural collapse (Fig. S20). Taken together, these results demonstrate that the stability of Co_3O_4 is intrinsically dependent on the protection afforded by defect-confined Ir single atoms, which endow the catalyst with long-term robustness under acidic OER conditions. Overall, the activity and stability metrics of Ir_{SA}-Co_3O_4 place it among the leading Ir-based OER catalysts reported to date (Fig. S21 and Table S2), reflecting the reliability of the design strategy and the comprehensive performance advantages.

To probe the dynamic evolution of interfacial electronic behavior under anodic polarization, operando EIS was performed across a series of stepped potentials (1.35–1.55 V vs. RHE) in 0.5 M H_2SO_4. As shown in the Bode plots (Figs 4a and b), Ir_{SA}-Co_3O_4 exhibits a rapid decline in phase angle with increasing potential. Notably, in the pre-OER regime, the reduced phase peak intensity, together with its shift toward higher frequencies, indicates enhanced charge accumulation in the inner Helmholtz layer and an earlier onset of surface polarization.[46] This response reflects the ability of the stabilized spinel framework to sustain capacitive charging, thereby enabling key elementary steps such as proton dissociation and electron transfer to proceed more readily near the OER threshold. In contrast, Ir_{ACSA}-Co_3O_4 and IrO_2 (Fig. S22) display broader and more sluggish phase transitions, consistent with hindered interfacial polarization. These observations are confirmed by the Nyquist plots (Fig. S13), where Ir_{SA}-Co_3O_4 consistently shows arcs with reduced radii, signifying lower charge-transfer resistance and more efficient charge transport at the electrolyte-electrode interface. By comparison, Ir_{ACSA}-Co_3O_4 and IrO_2 exhibit large semicircles with minimal shrinkage, indicating

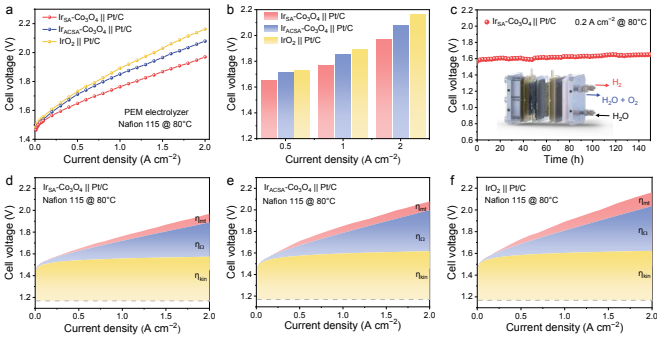

Fig. 5. Practical performance of Ir_{SA}-Co_3O_4 under PEMWE conditions. (a) Steady polarization curves of Ir_{SA}-Co_3O_4‖Pt/C, Ir_{ACSA}-Co_3O_4‖Pt/C, and IrO_2‖Pt/C for PEMWE. (b) Cell voltages at representative current densities (0.5, 1.0, and 2.0 A cm^{-2}). (c) Chronopotentiometry test conducted at 0.2 A cm^{-2} in a PEMWE electrolyzer at 80°C. (d-f) Voltage loss decomposition for the three devices, separating kinetic (η_{kin}), ohmic (η_Ω), and mass transport (η_{mt}) contributions.

persistent resistance and delayed electrochemical engagement. Taken together, the impedance results reveal that Ir_{SA}-Co_3O_4, by preserving the spinel lattice under acidic polarization, allows the intrinsic pseudocapacitive behavior of Co_3O_4 to be expressed, thereby accelerating interfacial polarization and advancing catalytic activation during the pre-OER stage.

The capacitive behavior derived from EIS fitting across the applied potential range (Figs. S23a-c) provides further insight into interfacial charge regulation. Ir_{SA}-Co_3O_4 exhibits the highest capacitance values (Fig. 4c), which gradually decrease with increasing potential, consistent with continuous charge storage and release at the interface. This profile reflects a responsive electrode surface that can sustain pseudocapacitive contributions under polarization.[47, 48] In contrast, Ir_{ACSA}-Co_3O_4 and IrO_2 exhibit significantly lower and nearly flat capacitance curves (Figs. 4d and S24), indicating limited adaptability and weak capacitive coupling. Pulse voltammetry was performed using sequential voltage steps with subsequent relaxation to examine the charge-current relationship (Figs. S25 and S26). The integration of the transient response yielded the accumulated charge. As shown in Fig. 4e, Ir_{SA}-Co_3O_4 presents a pronounced potential-dependent increase in both charge storage (Q) and current density (J), confirming efficient charge transfer and improved electronic conductivity under OER-relevant conditions.[49, 50] By comparison, Ir_{ACSA}-Co_3O_4 and IrO_2 (Fig. S27) exhibit a suppressed response, characterized by minimal charge accumulation and weak current growth, as the absence of a spatially defined Ir–O–Co configuration restricts interfacial polarization and charge transfer.

The above data indicate that variations in coordination environment dictate the extent to which the inherent pseudocapacitive behavior of Co_3O_4 is realized. Furthermore, DFT calculations were performed to estimate the Gibbs free energy changes of the OER steps, with a focus on activity differences at individual Ir sites (Figs. S28-S30). As shown in Fig. 4f, both Ir_{SA}-Co_3O_4 and Ir_{AC}-Co_3O_4 follow the adsorption-evolution mechanism (AEM), with the formation of *OOH serving as the potential-determining step. The 0.44 eV reduction in the limiting step indicates that the coordination environment created by Ir single-atom anchoring modulates intermediate adsorption, thereby lowering the kinetic barrier. Collectively, the experimental and theoretical results demonstrate that the coordination environment established by Ir single-atom anchoring plays a central role in promoting favorable reaction kinetics.

To evaluate the practical performance under PEMWE conditions, single-cell MEAs were fabricated using the CCM method.[51] Ir_{SA}-Co_3O_4, Ir_{ACSA}-Co_3O_4, and commercial IrO_2 were employed as OER anode catalysts, while commercial Pt/C was used as the HER cathode catalyst. All cells were operated at 80 °C with Nafion 115 serving as the proton-conducting membrane. As shown in Fig. 5a, Ir_{SA}-Co_3O_4‖Pt/C consistently delivered lower cell voltages across the full current density range. At 2.0 A cm^{-2}, the voltage reached 1.97 V, which was 0.11 V and 0.19 V lower than Ir_{ACSA}-Co_3O_4‖Pt/C and IrO_2‖Pt/C, respectively (Fig. 5b). Durability was further assessed by continuous electrolysis at 0.5 A cm^{-2}, where Ir_{SA}-Co_3O_4‖Pt/C maintained a stable cell voltage for 150 h with a voltage decay rate below 0.56 mV h^{-1} (Fig. 5c), which demonstrates robust operation under device-level conditions.

To clarify the origin of the voltage differences, overpotential decomposition was performed to separate kinetic, ohmic, and mass-transport contributions (Figs. 5d-f).[52] As summarized in Fig. S31, both kinetic and ohmic losses were markedly reduced for Ir_{SA}-Co_3O_4. The lower kinetic overpotential stems from optimized intermediate adsorption that accelerates reaction kinetics. The diminished ohmic component arises from a stabilized Co_3O_4 framework, where preserved pseudocapacitive behavior facilitates efficient charge storage and transfer across the catalyst-membrane interface. Mass-transport losses showed only minor variation, though Ir_{SA}-Co_3O_4 retained a slight advantage at high currents, consistent with its more dispersed nanoscale architecture that more readily accommodates gas release and alleviates local concentration buildup. These results demonstrate that the reduced voltage of Ir_{SA}-Co_3O_4 arises from the combined suppression of kinetic and ohmic losses, consistent with previous mechanistic understanding. Taken together, the findings suggest that Ir_{SA}-Co_3O_4 holds considerable potential for PEMWE, providing a rational basis for further development toward practical energy conversion technologies.

Conclusion

In summary, we have constructed a defect-mediated Ir single-atom catalyst by regulating the anchoring environment within the spinel Co_3O_4 support, enabling catalytic activity and structural robustness under acidic OER conditions. The well-defined Ir–O–Co coordination environment modulates electronic interactions that not only enhance the catalytic activity of Ir sites but also improve their resistance to dissolution under acidic conditions. In parallel, the constructed Ir–O–Co configuration couples Ir single-atom sites with the charge-accumulating capacity of Co_3O_4, thereby promoting early polarization and efficient charge transfer, thereby accelerating reaction kinetics. As a result, Ir_{SA}-Co_3O_4 delivers a low overpotential of 199 mV at 10 mA cm^{-2} in 0.5 M H2SO4 and maintains stable operation for over 300 h.

View Article Online
DOI: 10.1039/D5QI02279G

Under PEMWE conditions, the Ir_{SA}-Co_3O_4‖Pt/C cell exhibits stable operation over 150 h at 0.2 A cm^{-2}, with a voltage decay rate below 0.56 mV h^{-1}. This work provides a strategy to address the trade-off between activity and stability of SACs in acidic OER.

Author contributions

Yijun Xiang: Writing – original draft, Writing – review & editing, Formal analysis, Data curation. Hui Wang: Experimental assistance. Shaoxiong Li and Linlin Li: Visualization, Data analysis. Jianwei Ren and Gengyu Xing: Result discussion. Liming Deng and Shengjie Peng: Supervision, Funding acquisition.

Conflicts of interest

The authors declare no conflict of interest.

Acknowledgements

This work was supported by the National Natural Science Foundation of China (92472117, 22402081, 22509085, and 52371226), the Natural Science Foundation of Jiangsu Province (BK20210311, BK20221482, and BK20251369), the China National Postdoctoral Program for Innovative Talents (BX20250441), the China Postdoctoral Science Foundation (2025M774272), and the Jiangsu Funding Program for Excellent Postdoctoral Talent.

Notes and references

1. Z. W. Seh, J. Kibsgaard, C. F. Dickens, I. Chorkendorff, J. K. Nørskov, and T. F. Jaramillo, Combining theory and experiment in electrocatalysis: Insights into materials design, Science, 2017, **355**, eaad4998.
2. J. Zhang, X. Fu, S. Kwon, K. Chen, X. Liu, J. Yang, H. Sun, Y. Wang, T. Uchiyama, Y. Uchimoto, S. Li, Y. Li, X. Fan, G. Chen, F. Xia, J. Wu, Y. Li, Q. Yue, L. Qiao, D. Su, H. Zhou, W. A. Goddard, and Y. Kang, Tantalum-stabilized ruthenium oxide electrocatalysts for industrial water electrolysis, Science, 2025, **387**, 48-55.
3. S. Liu, Y. Shuai, X. Qi, Z. Ding, and Y. Liu, Unlocking high-efficiency oxygen evolution reaction through Co-N coordination engineering in Co@N-doped porous carbon core-shell nanoparticles, Nano Res., 2024, **17**, 7068-7076.
4. S. Kong, A. Li, J. Long, K. Adachi, D. Hashizume, Q. Jiang, K. Fushimi, H. Ooka, J. Xiao, and R. Nakamura, Acid-stable manganese oxides for proton exchange membrane water electrolysis, Nat. Catal., 2024, **7**, 252-261.
5. L. Deng, H. Chen, S.-F. Hung, Y. Zhang, H. Yu, H.-Y. Chen, L. Li, and S. Peng, Lewis acid-mediated interfacial water supply for sustainable proton exchange membrane water electrolysis, J. Am. Chem. Soc., 2024, **146**, 35438-35448.
6. J. Cao, D. Zhang, B. Ren, P. Song, and W. Xu, Tungsten single atoms incorporated in cobalt spinel oxide for highly efficient electrocatalytic oxygen evolution in acid, Energy Environ. Sci., 2024, **17**, 5911-5921.
7. L. Wu, Q. Liang, J. Zhao, J. Zhu, H. Jia, W. Zhang, P. Cai, and W. Luo, A Bi-doped RuO_2 catalyst for efficient and durable acidic water oxidation, Chin. J. Catal., 2023, **55**, 182-190.
8. G. Yu, R. Li, Y. Zhang, X. Lin, G. Wang, and X. Hong, Constructing high coordination number of Ir-O-Ru bonds in $IrRuO_x$ nanomeshes for highly stable acidic oxygen evolution reaction, Nano Res., 2024, **17**, 5073-5079.
9. J. Liang, C. Fu, S. Hwang, C. Dun, L. Luo, Z. Shadike, S. Shen, J. Zhang, H. Xu, and G. Wu, Constructing highly porous low iridium anode catalysts via dealloying for proton exchange membrane water electrolyzers, Adv. Mater., 2025, **37**, 2409386.
10. H. Zhou, J. Ban, Y. Shen, Y. Ning, S. Zhang, F. Liu, G. Cao, G. Shao, S. R. P. Silva, and J. Hu, Strategies to maximize the oxygen evolution reaction in layered double hydroxides by electronic defect engineering, eScience, 2025, **5**, 100380.
11. W. Shi, T. Shen, C. Xing, K. Sun, Q. Yan, W. Niu, X. Yang, J. Li, C. Wei, R. Wang, S. Fu, Y. Yang, L. Xue, J. Chen, S. Cui, X. Hu, K. Xie, X. Xu, S. Duan, Y. Xu, and B. Zhang, Ultrastable supported oxygen evolution electrocatalyst formed by ripening-induced embedding, Science, 2025, **387**, 791-796.
12. A. Li, S. Kong, K. Adachi, H. Ooka, K. Fushimi, Q. Jiang, H. Ofuchi, S. Hamamoto, M. Oura, K. Higashi, T. Kaneko, T. Uruga, N. Kawamura, D. Hashizume, and R. Nakamura, Atomically dispersed hexavalent iridium oxide from MnO_2 reduction for oxygen evolution catalysis, Science, 2024, **384**, 666-670.
13. F. Ikram, S. Cheong, I. Persson, Z. R. Ramadhan, A. R. Poerwoprajitno, J. J. Gooding, and R. D. Tilley, Iridium nanocrystals enriched with defects and atomic steps to enhance oxygen evolution reaction performance, J. Am. Chem. Soc., 2025, **147**, 10784-10790.
14. Z. Chen, X. Duan, W. Wei, S. Wang, and B.-J. Ni, Iridium-based nanomaterials for electrochemical water splitting, Nano Energy, 2020, **78**, 105270.
15. J. Chen, J. Ma, T. Huang, Q. Liu, X. Liu, R. Luo, J. Xu, X. Wang, T. Jiang, H. Liu, Z. Lv, T. Yao, G. Wang, X. Zheng, Z. Li, and W. Chen, Iridium-free high-entropy alloy for acidic water oxidation at high current densities, Angew. Chem. Int. Ed., 2025, **64**, e202503330.
16. H. Wang, Z. Yan, F. Cheng, and J. Chen, Advances in noble metal electrocatalysts for acidic oxygen evolution reaction: construction of under-coordinated active sites, Adv. Sci., 2024, **11**, 2401652.
17. B. Qiao, A. Wang, X. Yang, L. F. Allard, Z. Jiang, Y. Cui, J. Liu, J. Li, and T. Zhang, Single-atom catalysis of CO oxidation using Pt_1/FeO_x, Nat. Chem., 2011, **3**, 634-641.
18. R. Bai, Y. Yao, Q. Lin, L. Wu, Z. Li, H. Wang, M. Ma, D. Mu, L. Hu, H. Yang, W. Li, S. Zhu, X. Wu, X. Rui, and Y. Yu, Preferable single-atom catalysts enabled by natural language processing for high energy density Na-S batteries, Nat. Commun., 2025, **16**, 5827.
19. M. Qi, X. Du, X. Shi, S. Wang, B. Lu, J. Chen, S. Mao, H. Zhang, and Y. Wang, Single-atom Ru-triggered lattice oxygen redox mechanism for enhanced acidic water oxidation, J. Am. Chem. Soc., 2025, **147**, 18295-18306.

20. S. Li, G. Xing, S. Zhao, J. Peng, L. Zhao, F. Hu, L. Li, J. Wang, S. Ramakrishna, and S. Peng, Fe-N co-doped carbon nanofibers with Fe_3C decoration for water activation induced oxygen reduction reaction, Natl. Sci. Rev., 2024, **11**, nwae193.
21. J. Wang, S.-J. Kim, J. Liu, Y. Gao, S. Choi, J. Han, H. Shin, S. Jo, J. Kim, F. Ciucci, H. Kim, Q. Li, W. Yang, X. Long, S. Yang, S.-P. Cho, K. H. Chae, M. G. Kim, H. Kim, and J. Lim, Redirecting dynamic surface restructuring of a layered transition metal oxide catalyst for superior water oxidation, Nat. Catal., 2021, **4**, 212-222.
22. W. Song, K. Peng, W. Xu, X. Liu, H. Zhang, X. Liang, B. Ye, H. Zhang, Z. Yang, L. Wu, X. Ge, and T. Xu, Upscaled production of an ultramicroporous anion-exchange membrane enables long-term operation in electrochemical energy devices, Nat. Commun., 2023, **14**, 2732.
23. Y. Wang, H. Yan, and H. Fu, Recent advances and modulation tactics in Ru- and Ir-based electrocatalysts for PEMWE anodes at large current densities, eScience, 2025, **5**, 100323.
24. S. Ajmal, A. Rasheed, W. Sheng, G. Dastgeer, Q. A. T. Nguyen, P. Wang, P. Chen, S. Liu, V. Q. Bui, M. Zhu, P. Li, and D. Wang, Synergetic modulation of electronic properties of cobalt oxide via "Tb" single atom for uphill urea and water electrolysis, Adv. Mater., 2025, **37**, 2412173.
25. D. Zhou, J. Yu, J. Tang, X.-Y. Li, and P. Ou, Octahedral Co^{2+}-O-Co^{3+} in mixed cobalt spinel promotes active and stable acidic oxygen evolution, Adv. Energy Mater., 2025, **15**, 2404007.
26. X. Liu, L. Zhao, H. Xu, Q. Huang, Y. Wang, C. Hou, Y. Hou, J. Wang, F. Dang, and J. Zhang, Tunable cationic vacancies of cobalt oxides for efficient electrocatalysis in Li–O_2 Batteries, Adv. Energy Mater., 2020, **10**, 2001415.
27. Q. Hu, S. Qi, Q. Huo, Y. Zhao, J. Sun, X. Chen, M. Lv, W. Zhou, C. Feng, X. Chai, H. Yang, and C. He, Designing efficient nitrate reduction electrocatalysts by identifying and optimizing active sites of Co-based spinels, J. Am. Chem. Soc., 2024, **146**, 2967-2976.
28. Y. Liu, X. Wu, H. Qu, G. Lu, Y. Chen, B. Lu, Y. Song, G. Zhou, and H.-M. Cheng, Regulating the local spin states in spinel oxides to promote the activity of Li-CO_2 batteries, Adv. Mater., 2025, **37**, 2411652.
29. W. Zhu, F. Yao, K. Cheng, M. Zhao, C.-J. Yang, C.-L. Dong, Q. Hong, Q. Jiang, Z. Wang, and H. Liang, Direct dioxygen radical coupling driven by octahedral ruthenium–oxygen–cobalt collaborative coordination for acidic oxygen evolution reaction, J. Am. Chem. Soc., 2023, **145**, 17995-18006.
30. J. Zhao, Y. Guo, Z. Zhang, X. Zhang, Q. Ji, H. Zhang, Z. Song, D. Liu, J. Zeng, C. Chuang, E. Zhang, Y. Wang, G. Hu, M. A. Mushtaq, W. Raza, X. Cai, and F. Ciucci, Out-of-plane coordination of iridium single atoms with organic molecules and cobalt–iron hydroxides to boost oxygen evolution reaction, Nat. Nanotechnol., 2025, **20**, 57-66.
31. L. Cai, Y. Liu, Y. Gao, B.-H. Zhao, J. Guan, X. Liu, B. Zhang, and Y. Huang, Atomically asymmetrical Ir−O−Co sites enable efficient chloride-mediated ethylene electrooxidation in neutral seawater, Angew. Chem. Int. Ed., 2025, **64**, e202417092.
32. Y. Gao, C. Yang, F. Sun, D. He, X. Wang, J. Chen, X. Zheng, R. Liu, H. Pan, and D. Wang, Ligand-tuning metallic sites in molecular complexes for efficient water oxidation, Angew. Chem. Int. Ed., 2025, **64**, e202415755.
33. Z. Zhang, P. Ma, C. Jia, W. Gao, M. Liu, K. N. Hui, M. Zuo, S. Zhou, and J. Zeng, Site-specific stabilizing effect of single atoms on spinel oxides for acidic oxygen evolution, eScience, 2025, 100402.
34. W. Chen, M. Yu, S. Liu, C. Zhang, S. Jiang, and G. Duan, Recent progress of Ru single-atom catalyst: synthesis, modification, and energetic applications, Adv. Funct. Mater., 2024, **34**, 2313307.
35. Y. Lu, T. Liu, C.-L. Dong, Y.-C. Huang, Y. Li, J. Chen, Y. Zou, and S. Wang, Tuning the selective adsorption site of biomass on Co_3O_4 by Ir single atoms for electrosynthesis, Adv. Mater., 2021, **33**, 2007056.
36. S.-Y. Lu, B. Huang, M. Sun, M. Luo, M. Jin, H. Yang, Q. Zhang, H. Liu, P. Zhou, Y. Chao, K. Yin, C. Shang, J. Wang, Y. Wang, F. Lv, L. Gu, and S. Guo, Synthetic tuning stabilizes a high-valence Ru single site for efficient electrolysis, Nat. Synth., 2024, **3**, 576-585.
37. A. Wang, J. Li, and T. Zhang, Heterogeneous single-atom catalysis, Nat. Rev. Chem., 2018, **2**, 65-81.
38. R. Lang, X. Du, Y. Huang, X. Jiang, Q. Zhang, Y. Guo, K. Liu, B. Qiao, A. Wang, and T. Zhang, Single-atom catalysts based on the metal–oxide interaction, Chem. Rev., 2020, **120**, 11986-12043.
39. N. Wang, P. Ou, R. K. Miao, Y. Chang, Z. Wang, S.-F. Hung, J. Abed, A. Ozden, H.-Y. Chen, H.-L. Wu, J. E. Huang, D. Zhou, W. Ni, L. Fan, Y. Yan, T. Peng, D. Sinton, Y. Liu, H. Liang, and E. H. Sargent, Doping shortens the metal/metal distance and promotes OH coverage in non-noble acidic oxygen evolution reaction catalysts, J. Am. Chem. Soc., 2023, **145**, 7829-7836.
40. S. Li, S. Zhao, S.-F. Hung, L. Deng, L. Wang, F. Shi, A. Dong, Y. Zhang, T.-Y. Chen, F. Hu, L. Li, S. Ramakrishna, Y. Wu, and S. Peng, Oxophilic sites mediated dynamic oxygen replenishment to stabilize lattice oxygen catalysis in acidic water oxidation, J. Am. Chem. Soc., 2025, **147**, 33770-33779.
41. W. Yang, I. Y. Chernyshov, R. K. A. van Schendel, M. Weber, C. Müller, G. A. Filonenko, and E. A. Pidko, Robust and efficient hydrogenation of carbonyl compounds catalysed by mixed donor Mn(I) pincer complexes, Nat. Commun., 2021, **12**, 12.
42. R. Li, H. Wang, F. Hu, K. C. Chan, X. Liu, Z. Lu, J. Wang, Z. Li, L. Zeng, Y. Li, X. Wu, and Y. Xiong, IrW nanochannel support enabling ultrastable electrocatalytic oxygen evolution at 2 A cm^{-2} in acidic media, Nat. Commun., 2021, **12**, 3540.
43. M. Kunitski, N. Eicke, P. Huber, J. Köhler, S. Zeller, J. Voigtsberger, N. Schlott, K. Henrichs, H. Sann, F. Trinter, L. P. H. Schmidt, A. Kalinin, M. S. Schöffler, T. Jahnke, M. Lein, and R. Dörner, Double-slit photoelectron interference in strong-field ionization of the neon dimer, Nat. Commun., 2019, **10**, 1.
44. J. Dong, Y. Liu, J. Pei, H. Li, S. Ji, L. Shi, Y. Zhang, C. Li, C. Tang, J. Liao, S. Xu, H. Zhang, Q. Li, and S. Zhao, Continuous electroproduction of formate via CO_2 reduction on local symmetry-broken single-atom catalysts, Nat. Commun., 2023, **14**, 6849.

View Article Online
DOI: 10.1039/D5QI02279G

45. Z. Wang, X. Guo, J. Montoya, and J. K. Nørskov, Predicting aqueous stability of solid with computed Pourbaix diagram using SCAN functional, npj Comput. Mater., 2020, **6**, 160.
46. H.-Y. Wang, S.-F. Hung, H.-Y. Chen, T.-S. Chan, H. M. Chen, and B. Liu, In operando identification of geometrical-site-dependent water oxidation activity of spinel Co_3O_4, J. Am. Chem. Soc., 2016, **138**, 36-39.
47. Y. Li, W. Ma, J. Wang, and Q. Zhong, A NiFe-based monolithic electrocatalyst for pleiotropic-efficiency water oxidation, J. Mater. Chem. A, 2022, **10**, 24388-24397.
48. C. Wang, C. Deng, P. Zhai, X. Shi, W. Liu, D. Jin, B. Shang, J. Gao, L. Sun, and J. Hou, Tracking the correlation between spintronic structure and oxygen evolution reaction mechanism of cobalt-ruthenium-based electrocatalyst, Nat. Commun., 2025, **16**, 215.
49. Y. Dai, J. Yu, J. Wang, Z. Shao, D. Guan, Y.-C. Huang, and M. Ni, Bridging the charge accumulation and high reaction order for high-rate oxygen evolution and long stable Zn-Air batteries, Adv. Funct. Mater., 2022, **32**, 2111989.
50. H. N. Nong, L. J. Falling, A. Bergmann, M. Klingenhof, H. P. Tran, C. Spöri, R. Mom, J. Timoshenko, G. Zichittella, A. Knop-Gericke, S. Piccinin, J. Pérez-Ramírez, B. R. Cuenya, R. Schlögl, P. Strasser, D. Teschner, and T. E. Jones, Key role of chemistry versus bias in electrocatalytic oxygen evolution, Nature, 2020, **587**, 408-413.
51. Z. Shi, J. Li, J. Jiang, Y. Wang, X. Wang, Y. Li, L. Yang, Y. Chu, J. Bai, J. Yang, J. Ni, Y. Wang, L. Zhang, Z. Jiang, C. Liu, J. Ge, and W. Xing, Enhanced acidic water oxidation by dynamic migration of oxygen species at the Ir/Nb_2O_{5-x} catalyst/support interfaces, Angew. Chem. Int. Ed., 2022, **61**, e202212341.
52. L. Tao, F. Lv, D. Wang, H. Luo, F. Lin, H. Gong, H. Mi, S. Wang, Q. Zhang, L. Gu, M. Luo, and S. Guo, Mass-efficient catalyst layer of hierarchical sub-nanosheets on nanowire for practical proton exchange membrane electrolyzer, Joule, 2024, **8**, 450-460.

View Article Online
DOI: 10.1039/D5QI02279G

Data availability statements

The data supporting this article have been included as part of the Supplementary Information.